

1 **Long term variations of actual evapotranspiration over the Tibetan**  
2 **Plateau**

3 Cunbo Han<sup>1,2,3</sup>, Yaoming Ma<sup>1,4,5,6</sup>, Binbin Wang<sup>1,2</sup>, Lei Zhong<sup>7</sup>, Weiqiang  
4 Ma<sup>1,2,4</sup>, Xuelong Chen<sup>1,2,4</sup>, Zhongbo Su<sup>8</sup>

5 1. Key Laboratory of Tibetan Environment Changes and Land Surface  
6 Processes, Institute of Tibetan Plateau Research, Chinese Academy of  
7 Sciences, Beijing, China

8 2. Land-Atmosphere Interaction and its Climatic Effects Group, State Key  
9 Laboratory of Tibetan Plateau Earth System Science, Institute of Tibetan  
10 Plateau Research, Chinese Academy of Sciences, Beijing, China

11 3. Institute for Meteorology and Climate Research, Karlsruhe Institute of  
12 Technology, Karlsruhe, Germany

13 4. CAS Center for Excellence in Tibetan Plateau Earth Sciences, Chinese  
14 Academy of Sciences, Beijing, China

15 5. University of Chinese Academy of Sciences, Beijing, China

16 6. Lanzhou University, Lanzhou, China

17 7. Laboratory for Atmospheric Observation and Climate Environment  
18 Research, School of Earth and Space Sciences, University of Science  
19 and Technology of China, Hefei, China

20 8. Faculty of Geo-Information Science and Earth Observation, University of  
21 Twente, Enschede, The Netherlands

22

23 **Correspondence to:**

24 Prof. Dr. Yaoming Ma

25 Institute of Tibetan Plateau Research, Chinese Academy of Sciences

26 16-3 Lincui Road, Chaoyang District, Beijing, 100101, China

27 Tel: +86 010 84097079

28 Email: [ymma@itpcas.ac.cn](mailto:ymma@itpcas.ac.cn)

Deleted: ir

Deleted: e

31 **Abstract**

32 Terrestrial actual evapotranspiration ( $ET_a$ ) is a key parameter controlling land-  
33 atmosphere interaction processes and water cycle. However, spatial  
34 distribution and temporal changes of  $ET_a$  over the Tibetan Plateau (TP)  
35 remain very uncertain. Here we estimate the multiyear (2001-2018) monthly  
36  $ET_a$  and its spatial distribution on the TP by a combination of meteorological  
37 data and satellite products. Validation against data from six eddy-covariance  
38 monitoring sites yielded root-mean-square errors ranging from 9.3 to 14.5 mm  
39  $mo^{-1}$ , and correlation coefficients exceeding 0.9. The domain mean of annual  
40  $ET_a$  on the TP decreased slightly ( $-1.45 \text{ mm yr}^{-1}$ ,  $p < 0.05$ ) from 2001 to 2018.  
41 The annual  $ET_a$  increased significantly at a rate of  $2.62 \text{ mm yr}^{-1}$  ( $p < 0.05$ ) in  
42 the eastern sector of the TP ( $lon > 90^\circ \text{ E}$ ), but decreased significantly at a rate  
43 of  $-5.52 \text{ mm yr}^{-1}$  ( $p < 0.05$ ) in the western sector of the TP ( $lon < 90^\circ \text{ E}$ ). In  
44 addition, the decreases in annual  $ET_a$  were pronounced in spring and summer  
45 seasons, while almost no trends were detected in the autumn and winter  
46 seasons. The mean annual  $ET_a$  during 2001-2018 and over the whole TP was  
47  $496 \pm 23 \text{ mm}$ . Thus, the total evapotranspiration from the terrestrial surface of  
48 the TP was  $1238.3 \pm 57.6 \text{ km}^3 \text{ yr}^{-1}$ . The estimated  $ET_a$  product presented in  
49 this study is useful for an improved understanding of changes in energy and  
50 water cycle on the TP. The dataset is freely available at the Science Data  
51 Bank (<http://www.dx.doi.org/10.11922/sciencedb.t00000.00010>, (Han et al.,  
52 2020)) and at the National Tibetan Plateau Data Center  
53 (<https://data.tpdac.ac.cn/en/data/5a0d2e28-ebc6-4ea4-8ce4-a7f2897c8ee6/>).

54

55 **Key words:** Actual evapotranspiration; SEBS; Tibetan Plateau; Trend.

56

57

58 **Key points:**

- 59     • The SEBS-estimated monthly  $ET_a$  during 2001-2018 has been  
60         validated against 6 flux towers on the TP.
- 61     • Annual  $ET_a$  over the entire TP and in the western TP decrease  
62         significantly, while it increases in the eastern TP.
- 63     • Decrease of annual  $ET_a$  is pronounced in spring and summer, while  
64         almost no trends are detected in autumn and winter.

65

66

67 **1 Introduction**

68 As the birthplace of Asia's major rivers, the Tibetan Plateau (TP), famous as  
69 the "Water Tower of Asia", is essential to the Asian energy and water cycles  
70 ([Immerzeel et al., 2010](#); [Yao et al., 2012](#)). Along with increasing air  
71 temperature, evidence from the changes of precipitation, runoff, and soil  
72 moisture indicates that the hydrological cycle of the TP has been intensified  
73 during the past century ([Yang et al., 2014](#)). Consuming around two-thirds of  
74 global terrestrial precipitation, evapotranspiration (*ET*) is a crucial component  
75 that affects the exchange of water and energy between the land surface and  
76 the atmosphere ([Oki and Kanae, 2006](#); [Fisher et al., 2017](#)). *ET* is also a key  
77 factor modulating regional and global weather and climate. As one essential  
78 connecting component between the energy budget and the water cycle in the  
79 terrestrial ecosystems ([Xu and Singh, 2005](#)), *ET* and its variations have been  
80 drawing more attention worldwide ([Xu and Singh, 2005](#); [Li et al., 2014](#); [Zhang](#)  
81 [et al., 2018b](#); [Yao et al., 2019](#); [Wang et al., 2020b](#)). Total evaporation from  
82 large lakes of the TP has been quantitatively estimated recently ([Wang et al.,](#)  
83 [2020a](#)), however, the terrestrial *ET* on the TP and its spatial and temporal  
84 changes remain very uncertain.

85

86 Many studies have tried to evaluate *ET*'s temporal and spatial variability  
87 across the TP using various methods. The pan evaporation ( $E_{\text{pan}}$ ), that  
88 represents the amount of water evaporated from an open circular pan, is the  
89 most popular observational data source of *ET*. Long time series of  $E_{\text{pan}}$  are  
90 often available with good comparability among various regional  
91 measurements. Thus, it has been widely used in various disciplines, e.g.,  
92 meteorology, hydrology, and ecology. Several studies have revealed the trend  
93 of  $E_{\text{pan}}$  on the TP ([Zhang et al., 2007](#); [Liu et al., 2011](#); [Shi et al., 2017](#); [Zhang](#)  
94 [et al., 2018a](#); [Yao et al., 2019](#)). Although  $E_{\text{pan}}$  and potential *ET* suggest the

95 long-term variability of  $ET$  according to the complementary relationship (CR)  
96 between  $E_{pan}$  and actual  $ET$  ( $ET_a$ ) ([Zhang et al., 2007](#)), these measures  
97 cannot precisely depict the spatial pattern of trends in  $ET_a$ . Recently, several  
98 studies applied revised models, which are based on the CR of  $ET$ , to estimate  
99  $ET_a$  on the TP ([Zhang et al., 2018b](#); [Ma et al., 2019](#); [Wang et al., 2020b](#)).  
100 Employing only routine meteorological observations without requiring any  
101 vegetation and soil information is the most significant advantage of CR  
102 models ([Szilagyi et al., 2017](#)). However, numerous assumptions and  
103 requirements of validations of key parameters limit the application and  
104 performance of CR models over different climate conditions. The application  
105 of eddy-covariance (EC) technologies in the past decade has dramatically  
106 advanced our understanding of the terrestrial energy balance and  $ET_a$  over  
107 various ecosystems across the TP. However, the fetch of the EC observation  
108 is on the order of hundreds of meters, thus impeding the ability to capture the  
109 plateau-scale variations of  $ET_a$ . Therefore, finding an effective way to advance  
110 the estimation of  $ET_a$  on the TP is of great importance.

111

112 Satellite remote sensing (RS) provides temporally frequent and spatially  
113 contiguous measurements of land surface characteristics that affect  $ET$ , for  
114 example, land surface temperature, albedo, vegetation index. Satellite RS  
115 also offers the opportunity to retrieve  $ET$  over a heterogeneous surface  
116 ([Zhang et al., 2010](#)). Multiple RS-based algorithms have been proposed.  
117 Among these algorithms, the surface energy balance system (SEBS)  
118 proposed by [Su \(2002\)](#) has been widely applied to retrieve land surface  
119 turbulent fluxes on the TP ([Chen et al., 2013b](#); [Ma et al., 2014](#); [Han et al.,](#)  
120 [2016](#); [Han et al., 2017](#); [Zou et al., 2018](#); [Zhong et al., 2019](#)). [Chen et al.](#)  
121 [\(2013b\)](#) improved the roughness length parameterization scheme for heat  
122 transfer in SEBS to expand its modeling applicability over bare ground, sparse

123 canopy, dense canopy, and snow surfaces in the TP. An algorithm for effective  
124 aerodynamic roughness length had been introduced into the SEBS model to  
125 parameterize subgrid-scale topographical form drag ([Han et al., 2015](#); [Han et  
126 al., 2017](#)). This scheme improved the skill of the SEBS model in estimating  
127 the surface energy budget over mountainous regions of the TP. A recent  
128 advance by [Chen et al. \(2019\)](#) optimized five critical parameters in SEBS  
129 using observations collected from 27 sites globally, including 6 sites on the TP,  
130 and suggested that the overestimation of the global  $ET$  was substantially  
131 improved with the use of optimal parameters.

132

133 While the spatial and temporal pattern of the  $ET_a$  in the TP had been  
134 investigated in many studies ([Zhang et al., 2007](#); [Zhang et al., 2018b](#); [Wang  
135 et al., 2020b](#)), considerable inconsistencies for both trends and magnitudes of  
136  $ET_a$  exist due to uncertainties in forcing and parameters used by various  
137 models. Thus, in this study, with full consideration of the recent developments  
138 in the SEBS model over the TP, we aim to (1) develop an 18-year (2001-2018)  
139  $ET_a$  product of the TP, along with independent validations against EC  
140 observations; (2) quantify the spatiotemporal variability of the  $ET_a$  in the TP,  
141 and (3) uncover the main factors dominating the changes in  $ET_a$ , using the  
142 estimated product.

143

## 144 **2 Methodology and data**

### 145 **2.1 Model description**

146 The SEBS model ([Su, 2002](#)) was used to derive land surface energy flux  
147 components in the present study. The remote-sensed land surface energy  
148 balance equation is given by

149 
$$R_n = H + LE + G_0. \quad (1)$$

150  $R_n$  is net radiation flux ( $W\ m^{-2}$ ),  $H$  is sensible heat flux ( $W\ m^{-2}$ ),  $LE$  is latent  
151 heat flux ( $W\ m^{-2}$ ), and  $G_0$  is ground heat flux ( $W\ m^{-2}$ ). Note that this equation  
152 neglected energy stored in the canopy, energy consumption related to freeze-  
153 thaw processes of permafrost and glacier, etc. This equation is not applicable  
154 to any condition where a phase change of water occurs, except the liquid to  
155 vapour phase change.

**Deleted:** Thus, this equation is applicable without considering the phase change of water

156  
157 The land surface net radiation flux was computed as

158 
$$R_n = (1 - \alpha) \times SWD + LWD - \varepsilon \times \sigma \times T_s^4 \quad (2)$$

159 where  $\alpha$  is the land surface albedo derived from the Moderate Resolution  
160 Imaging Spectroradiometer (MODIS) products. Downward shortwave ( $SWD$ )  
161 and longwave ( $LWD$ ) radiation were obtained from the China Meteorological  
162 Forcing Dataset (CMFD). Land surface temperature ( $T_s$ ) and emissivity ( $\varepsilon$ )  
163 values were also obtained from MODIS products.

164  
165 In vegetated areas the soil heat flux,  $G_0$ , was calculated from the net radiation  
166 flux and vegetation cover

167 
$$G_0 = R_n \times (r_c \times f_c + r_s \times (1 - f_c)). \quad (3)$$

168  $r_s$  and  $r_c$  are ratios of ground heat flux and net radiation for surfaces with bare  
169 soil and full vegetation, respectively. Fractional vegetation cover ( $f_c$ ) was  
170 derived from the normalized difference vegetation index (NDVI). Over water  
171 surfaces (NDVI < 0 and  $\alpha < 0.47$ ),  $G_0 = 0.5R_n$  was used ([Gao et al., 2011](#);  
172 [Chen et al., 2013a](#)). On glaciers,  $G_0$  is negligible ([Yang et al., 2011](#)) and  $G_0 =$   
173  $0.05R_n$ .

174  
175 In the atmospheric surface layer, sensible heat flux and friction velocity were  
176 calculated based on the Monin-Obukhov similarity ([Stull, 1988](#)),

179 
$$U = \frac{u_*}{\kappa} \left[ \ln \left( \frac{z-d_0}{z_{0m}^{eff}} \right) - \psi_m \left( \frac{z-d_0}{L} \right) + \psi_m \left( \frac{z_{0m}^{eff}}{L} \right) \right] \quad (4)$$

180 
$$\theta_0 - \theta_a = \frac{H}{\kappa u_* \rho C_p} \left[ \ln \left( \frac{z-d_0}{z_{0h}^{eff}} \right) - \psi_h \left( \frac{z-d_0}{L} \right) + \psi_h \left( \frac{z_{0h}^{eff}}{L} \right) \right] \quad (5)$$

181 
$$L = \frac{\rho C_p u_*^2 \theta_v}{\kappa g H}. \quad (6)$$

182  $U$  is the horizontal wind velocity at a reference height  $z$  (m) above the ground  
 183 surface,  $\theta_0$  is the potential temperature at the land surface (K),  $\theta_a$  is the  
 184 potential temperature (K) at the reference height  $z$ ,  $d_0$  is the zero-plane  
 185 displacement height (m),  $\rho$  is the air density ( $\text{kg m}^{-3}$ ),  $C_p$  is the specific heat for  
 186 moist air ( $\text{J kg}^{-1} \text{ }^\circ\text{C}^{-1}$ ),  $\kappa = 0.4$  is the von Kármán's constant,  $u_*$  is the friction  
 187 velocity,  $L$  is the Monin-Obukhov length (m),  $\theta_v$  is the potential virtual  
 188 temperature (K) at the reference height  $z$ ,  $\psi_m$  and  $\psi_h$  are the stability  
 189 correction functions for momentum and sensible heat transfer respectively,  
 190 and  $g$  is the gravity acceleration ( $\text{m s}^{-2}$ ). To account for the form drag caused  
 191 by subgrid-scale topographical obstacles, effective roughness lengths for  
 192 momentum ( $z_{0m}^{eff}$ , m) and sensible heat ( $z_{0h}^{eff}$ , m) transfer were introduced into  
 193 the SEBS model by [Han et al. \(2017\)](#). These modifications are parameterized  
 194 as follows ([Grant and Mason, 1990](#); [Han et al., 2015](#)),

195 
$$\ln^2 \left( \frac{h/2z_{0m}^{eff}}{h/2z_{0m}} \right) = \frac{\kappa^2}{0.5D\lambda + \kappa^2 / \ln^2(h/2z_{0m})} \quad (7)$$

196 
$$\ln \left( \frac{h/2z_{0h}^{eff}}{h/2z_{0h}} + 1 \right) = \ln \left( \frac{h/2z_{0h}}{h/2z_{0h}} + 1 \right) \frac{\ln(h/2z_{0m} + 1)}{\ln(h/2z_{0m}^{eff} + 1)} \quad (8)$$

197 where  $h$  is the average height of the subgrid-scale roughness obstacles,  $\lambda$  is  
 198 the average density of the subgrid-scale roughness elements calculated from  
 199 digital elevation models,  $D$  is the form drag coefficient and  $D=0.4$  is used for  
 200 the mountainous areas of the TP as suggested by [Han et al. \(2015\)](#),  $z_{0m}$  and  
 201  $z_{0h}$  are the local-scale roughness lengths for momentum (m) and heat transfer  
 202 (m), respectively. Detailed calculations can be found in [Su \(2002\)](#). A revised  
 203 algorithm for  $z_{0h}$  developed by [Chen et al. \(2013b\)](#) was applied as this  
 204 algorithm outperforms the original scheme of the SEBS model on the TP.

205



206 To constraint the actual evapotranspiration, the evaporative fraction was  
207 applied in the SEBS model, which is determined by taking energy balance  
208 considerations at dry and wet limiting cases. Under the dry-limit condition, the  
209 evaporation becomes zero due to the limited supply of available soil moisture,  
210 while water vapor evaporates at the potential rate under the wet-limit condition  
211 ([Su, 2002](#)). The evaporative fraction ( $\Lambda$ ) is defined as,

$$212 \quad \Lambda = \frac{LE}{R_n - G_0} \quad (9)$$

213 After calculating evaporative fraction based on the assumption of dry and wet  
214 limits, latent heat flux was calculated by inverting Equation (9). Finally, latent  
215 heat flux was converted to  $ET_a$ . Details are available in [Su \(2002\)](#) and [Chen  
216 et al., 2013a](#). Note that the dry-wet limit assumption did not apply to frozen  
217 soil, water, snow, and ice surfaces. The latent heat flux was obtained as the  
218 residual of the surface energy balance equation (1) after calculating net  
219 radiation, sensible heat flux, and ground heat flux when the dry-wet limit  
220 assumption is not applicable.

## 221 2.2 Data

222 In-situ observations, satellite-based products, and meteorological forcing data  
223 were used in this study to estimate monthly  $ET_a$  over the TP area. The CMFD,  
224 that was developed based on the released China Meteorological  
225 Administration (CMA) data ([He et al., 2020](#)), was used as model input. The  
226 CMFD covers the whole landmass of China at a spatial resolution of  $0.1^\circ$  and  
227 a temporal resolution of three hours. The CMFD dataset was established  
228 through the fusion of in-situ observations, remote sensing products, and  
229 reanalysis datasets. In particular, the dataset benefits from the merging of the  
230 observations at about 700 CMA's weather stations, and by using the Global  
231 Energy and Water Cycle Experiment – Surface Radiation Budget (GEWEX-  
232 SRB) shortwave radiation dataset ([Pinker and Laszlo, 1992](#)). The GEWEX-

233 SRB data has not been used in any other reanalysis dataset. In addition,  
234 independent datasets observed in western China where weather stations are  
235 scarce were used to evaluate the CMFD. This includes data collected through  
236 the Heihe Watershed Allied Telemetry Experimental Research (HiWATER) ([Li  
237 et al., 2013](#)) and the Coordinated Enhanced Observing Period (CEOP) Asia-  
238 Australia Monsoon Project (CAMP) ([Ma et al., 2003](#)). CMFD dataset has been  
239 validated against in situ meteorological observations and compared with other  
240 reanalysis datasets on the TP, demonstrating that it is one of the best  
241 meteorological forcing datasets over the TP area ([Zhou et al., 2016](#); [Xie et al.,  
242 2017](#); [Wang et al., 2020a](#)). Therefore, it is suitable for this study to drive the  
243 SEBS model. Detailed information for the CMFD dataset is listed in Table 1.

244

245 MODIS monthly land surface products, including land surface temperature  
246 and emissivity, land surface albedo, and vegetation index, provide land  
247 surface conditions for the SEBS model. Detailed information on MODIS land  
248 surface variables are listed in Table 1. The values of land surface variables in  
249 the MODIS monthly products are derived by compositing and averaging the  
250 values from the corresponding month of MODIS daily files. Validations of  
251 MODIS land surface temperature and albedo against in-situ observations on  
252 the TP suggesting a high quality of MODIS land surface products with low  
253 biases and small root-mean-square errors ([Wang et al., 2004](#); [Ma et al., 2011](#);  
254 [Chen et al., 2014](#)).

255

256 In-situ EC data observed at six flux stations on the TP were used to validate  
257 model results. Locations of the six observation sites are illustrated in Figure 1  
258 and detailed descriptions for these six sites are shown in Table 2. The  
259 instrumental setup at each site consists of: an EC system comprising a sonic  
260 anemometer (CSAT3, Campbell Scientific Inc) and an open-path gas analyzer

261 (LI-7500, Li-COR); a four-component radiation flux system (CNR-1, Kipp &  
262 Zonen), installed at a height of 1.5 m; a soil heat flux plate (Hukseflux,  
263 HFP01), buried in the soil to a depth of 0.1 m; soil moisture and temperature  
264 probes, buried at a depth of 0.05, 0.10, and 0.15 m, respectively ([Han et al.,  
265 2017](#)). The EC data were processed with the EC software package TK3  
266 ([Mauder and Foken, 2015](#)). The main post-processing procedures of the EC  
267 raw data were as follows: spike detection, coordinate rotation, spectral loss  
268 correction, frequency response corrections ([Moore, 1986](#)), and corrections for  
269 density fluctuations ([Webb et al., 1980](#)). The ground heat flux was obtained by  
270 summing the flux value observed by the heat flux plate and the energy  
271 storage in the layer above the heat flux plate ([Han et al., 2016](#)). A more  
272 comprehensive dataset including the EC data used in this work has been  
273 published and is freely available ([Ma et al., 2020](#)).

274

275 3-hourly CMFD data was averaged into daily and then into monthly data to be  
276 consistent with MODIS products in terms of temporal resolution. Daily land  
277 surface albedo has been averaged into monthly variable. MODIS land surface  
278 products and canopy height data were remapped onto CMFD's grid. Monthly  
279 EC data and in situ meteorological observations, which are used for model  
280 validation, were generated from half-hourly variables.

### 281 **2.3 Model evaluation metrics and data analysis methods**

282 The model performance was assessed using the Pearson correlation  
283 coefficient (R), the root-mean-square error (RMSE), and the mean bias (MB)  
284 between the estimated and observed monthly  $ET_a$  at the six stations on the  
285 TP.

286

287 The least-square regression technique was used to detect the long-term linear

288 annual trends in  $ET_a$  values. The linear model to simulate  $ET_a$  values ( $Y_t$ )  
289 against time ( $t$ ) is defined as below and the slope of the linear equation ( $b$ ) is  
290 taken as the changing trend,

$$291 \qquad Y_t = Y_0 + bt + \varepsilon_t \qquad (10)$$

292

293 The Student's  $t$ -test, having an  $n-2$  degree of freedom ( $n$  is the number of  
294 samples), was used to evaluate the statistical significance of the linear  
295 trends, and only tests with a  $p$ -value less than 0.05 were selected as having  
296 passed the significance test.

### 297 **3 Results and discussion**

#### 298 **3.1 Validation against flux tower observations**

299 The SEBS-estimated  $ET_a$  was validated against EC observations at six flux  
300 stations on the TP at a monthly scale (Figure 2). The SEBS model is capable  
301 of capturing both the magnitude and seasonal variation of the monthly  $ET_a$   
302 signal at all the six stations. The correlation coefficients are all larger than 0.9  
303 and have passed the significance test at the  $p = 0.01$  level. RMSE values  
304 range from 9.3 to 14.5 mm mo<sup>-1</sup> with the minimum at the BJ station and the  
305 maximum at the SETORS station. The MB values are all negative except at  
306 the NADORS station, which means the SEBS model slightly underestimated  
307  $ET_a$  values on the TP.

308

309 Specifically, the SEBS model performed particularly well at the short grass  
310 sites (BJ and NAMORS), with correlation coefficients as high as 0.98 and MB  
311 values below 5.0 mm mo<sup>-1</sup>. At the high grass site (SETORS) and the gravel  
312 site (QOMS), the SEBS model is capable of reproducing the EC-observed  
313 monthly  $ET_a$  with RMSE values of 14.5 and 13.2 mm mo<sup>-1</sup>, respectively. In

314 addition, the underestimates of  $ET_a$  by SEBS are mostly in the dry season,  
315 when the canopy is withered. The validation at the site-scale indicates that the  
316 SEBS model used in this work can be applied to a wide range of ecosystems  
317 over the TP.

### 318 **3.2 Spatial distribution**

319 There was a clear spatial pattern to the multiyear average of annual  $ET_a$   
320 between 2001 and 2018 (Figure 3). In general, the SEBS-estimated  $ET_a$   
321 decreases from the southeast to the northwest of the TP, with the maximum  
322 value above 1200 mm in the southeastern Tibet and Hengduan Mountains  
323 and the minimum value less than 100 mm in the northwestern edge of the TP.  
324 In the central TP, where there are several lakes,  $ET_a$  was typically from 500 to  
325 1000 mm.  $ET_a$  was lower than 200 mm over the high, snow- and ice-bound,  
326 mountainous areas. For example, over the northern slopes of the Himalaya,  
327 Nyenchen Tanglha Mountains, and the eastern section of the Tanggula  
328 Mountains. The reason is that these snow- and ice-bound mountainous areas  
329 have a higher ability to reflect downward shortwave radiation and hence have  
330 less available energy to evaporate. On the whole, the domain averaged  
331 multiyear mean annual  $ET_a$  over the TP is  $496\pm 23$  mm. The total amount of  
332 water evapotranspired from the terrestrial surface of the TP are around  
333  $1238.3\pm 57.6$  km<sup>3</sup> yr<sup>-1</sup>, considering the area of the TP to be  $2.5\times 10^6$  km<sup>2</sup>.  
334

335 Figure 4 shows the multi-year average spring (March, April, and May), summer  
336 (June, July, and August), autumn (September, October, and November), and  
337 winter (December, January, and February)  $ET_a$  on the TP. Generally, the  
338 distribution pattern of seasonal  $ET_a$  was comparable with that of the annual  
339  $ET_a$ . Both seasonal and annual  $ET_a$  show a decreasing trend from the  
340 southeastern TP to the northwestern TP. Note that the spatial contrast of  $ET_a$

341 almost faded out in winter season owing to a minimum in available energy  
342 and precipitation (Figure 4d). The  $ET_a$  in spring is higher than that in autumn,  
343 except for some high mountainous areas (e.g.: mountain ranges of Himalaya  
344 and Hengduan mountains). The spring  $ET_a$  ranges from 50 mm to 450 mm,  
345 while autumn  $ET_a$  ranges from 50 mm to 250 mm. In summer, the  $ET_a$  is  
346 larger than 250 mm in most of the TP, while the  $ET_a$  is still below 100 mm in  
347 large areas of the northwestern TP. The multiyear seasonal  $ET_a$  averaged  
348 over the whole TP is  $140\pm 10$  mm,  $256\pm 12$  mm,  $84\pm 5$  mm, and  $34\pm 4$  mm, for  
349 spring, summer, autumn, and winter, respectively.

### 350 3.3 Trend analysis

351 The trend of annual  $ET_a$  during 2001-2018 is shown in Figure 5. Overall, an  
352 increasing trend of SEBS-simulated  $ET_a$  is dominant in the eastern TP (lon >  
353  $90^\circ$  E) while a decreasing trend is dominant in the western TP (lon <  $90^\circ$  E).  
354 The trends pass the  $t$ -test ( $p < 0.05$ ) in most part of the areas. The decreasing  
355 trend in the western TP is pronounced and passes the  $t$ -test ( $p < 0.05$ ). This  
356 trend is larger than  $-7.5$  mm  $yr^{-1}$  in most parts of the area and even larger than  
357  $-10$  mm  $yr^{-1}$  in a few parts. In the eastern TP, the increasing trend is mostly  
358 between 5 and 10 mm  $yr^{-1}$  and passes the  $t$ -test ( $p < 0.05$ ). The  $ET_a$  trend  
359 tends to be greater along the marginal region of the northern, eastern, and  
360 southeastern TP. Along the marginal region of the southwestern TP and in the  
361 western section of Himalaya Mountains this trend weakens.

362

363 The trends of seasonal  $ET_a$  between 2001 and 2018 are spatially  
364 heterogeneous over the TP (Figure 6). Decreasing trends in spring and  
365 summer are generally at a rate between  $-2.5$  and  $-7.5$  mm  $yr^{-1}$ , and increasing  
366 trends are generally at a rate below 5.0 mm  $yr^{-1}$  and 7.5 mm  $yr^{-1}$  in spring and  
367 summer, respectively. Areas showing decreasing  $ET_a$  tend to become larger in

368 autumn and winter seasons. Both the decreasing and increasing trends are  
369 subdued in autumn and winter compared with that in spring and summer  
370 seasons. Decreasing rates of  $ET_a$  in autumn and winter are generally below -  
371 2.5 mm yr<sup>-1</sup>, and only a few areas have a rate larger than -2.5 mm yr<sup>-1</sup>.

372

373 Due to the contrast in the trends in the eastern and western halves of the TP,  
374 we divided the TP into two regions: the eastern TP (lon > 90° E) and the  
375 western TP (lon < 90° E). Trends of the  $ET_a$  anomaly averaged over the entire  
376 TP, the western TP, and the eastern TP are shown in Figure 7a. The domain  
377 means of  $ET_a$  on the TP as a whole, and in the western TP decreased at rates  
378 of -1.45 mm yr<sup>-1</sup> and -5.52 mm yr<sup>-1</sup>, respectively. However, the  $ET_a$  in the  
379 eastern TP increased at a rate of 2.62 mm yr<sup>-1</sup>. The decreasing rate of  $ET_a$  in  
380 the entire TP is influenced mainly by the significant decrease of  $ET_a$  in the  
381 western TP. Seasonally, the rates of change of  $ET_a$  over the whole TP are -  
382 0.82 mm yr<sup>-1</sup> ( $p < 0.05$ ) and -0.79 mm yr<sup>-1</sup> ( $p < 0.05$ ) in spring and summer,  
383 respectively (Figure 7b). However, in autumn and winter the  $ET_a$  changes at a  
384 rate of 0.10 mm yr<sup>-1</sup> and 0.06 mm yr<sup>-1</sup>, respectively, and do not pass the  $t$ -test  
385 ( $p < 0.05$ ).  $ET_a$  in spring and summer seasons account for 75.7% of the  
386 annual  $ET_a$ . The variation in amplitude and changing rates in these two  
387 seasons are much larger than in the other seasons. Moreover, spatial  
388 distributions of spring and summer  $ET_a$  trends are close to that of the annual  
389  $ET_a$  trend (Figure 6). Thus, changes of  $ET_a$  in the spring and summer  
390 dominate the variations of  $ET_a$  in the whole year.

391

392 The decrease of  $ET_a$  over the whole TP and in the western TP during 2001-  
393 2018 can be explained by the decrease of  $R_n$  in the same time period (Figure  
394 8a). From 2001 to 2012,  $ET_a$  averaged over the entire TP increased slightly  
395 and then decreased dramatically from 2012, reaching a minimum in 2014.

396 The significant decrease in  $ET_a$  between 2012 and 2014 was due to the rapid  
397 decline of the  $R_n$  (Figure 8a). In the eastern TP,  $ET_a$  increased during 2001-  
398 2018, while  $R_n$  decreased in the same period. Thus,  $R_n$  was not the dominant  
399 factor controlling the annual variations of  $ET_a$ . However, the increasing trends  
400 of both precipitation and air temperature can explain the increase of  $ET_a$  in the  
401 eastern TP during the period 2001-2018 (Figure 8b and Figure 8c). The  
402 increasing precipitation increased the water resource available for  $ET_a$ .  
403 Moreover, the increasing air temperature accelerated the melting of  
404 permafrost and glaciers on the TP. Hence, the melting water replenished the  
405 ecosystem and increased the  $ET_a$  of the eastern TP.

406

407 Although the domain-averaged trend in  $ET_a$  has been decreasing across the  
408 entire TP from 2001 to 2018,  $ET_a$  values in some areas have increased.  
409 Moreover, the changing rates also depend on the time series of  $ET_a$ . For  
410 example, the  $ET_a$  increased slightly from 2001 to 2012, while decreased from  
411 2001 to 2018. This demonstrates the necessity to evaluate the spatial  
412 distribution of changing trends in  $ET_a$  and utilize long time series to investigate  
413 the trends in  $ET_a$  over the TP.

#### 414 **4 Summary and conclusions**

415 The SEBS-estimated  $ET_a$  is at a resolution of around 10 km, while the  
416 footprint of EC observed  $ET_a$  values ranges from a few dozen meters to a few  
417 hundreds of meters. SEBS-estimated  $ET_a$  compares very well with  
418 observations at the six flux towers, showing low RMSE and MB values. These  
419 estimates were able to capture annual and seasonal variations in  $ET_a$ , despite  
420 these two datasets being mismatched in their spatial representation. Note that  
421 the energy consumption related to freeze-thaw processes and sublimation is  
422 neglected. Thus, the dataset is likely to be less reliable over the glacier.



423 permafrost, and in winter season.

424

425 Heterogeneous land surface characteristics and nonlinear changes in  
426 atmospheric conditions resulted in heterogeneities in spatial distributions of  
427  $ET_a$  and changes in  $ET_a$ . The SEBS-estimated multiyear (2001-2018) mean  
428 annual  $ET_a$  on the TP was  $515 \pm 22$  mm, resulting in approximately  
429  $1287.5 \pm 55.0$  km<sup>3</sup> yr<sup>-1</sup> of total water evapotranspiration from the terrestrial  
430 surface. Annual  $ET_a$  generally decreased from the southeast to the northwest  
431 of the TP. The maximum was over 1200 mm, in the southeastern Tibet and  
432 Hengduan Mountains, while the minimum was less than 100 mm in the  
433 northwest marginal area of the TP. Moreover,  $ET_a$  was typically lower than 200  
434 mm over snow- and ice-bound mountainous areas, as there was limited  
435 available energy to evaporate the water.

436

437 Averaged over the entire TP, annual  $ET_a$  increased slightly from 2001 to 2012,  
438 but decreased significantly after 2012 and reached a minimum in 2014.

439 Generally, there was a slight decreasing trend in the domain mean annual  $ET_a$   
440 on the TP at the rate of  $-1.45$  mm yr<sup>-1</sup> ( $p < 0.05$ ) from 2001 to 2018. However,  
441 trends of annual  $ET_a$  were opposite in the western and eastern TP. The  
442 annual  $ET_a$  decreased significantly in the western TP at a rate of  $-5.52$  mm yr<sup>-1</sup>  
443 ( $p < 0.05$ ) from 2001 to 2018, while annual  $ET_a$  in the eastern TP increased  
444 at a rate of  $2.62$  mm yr<sup>-1</sup> ( $p < 0.05$ ) in the same period.

445

446 The spatial distributions of seasonal  $ET_a$  trends were also noticeably  
447 heterogeneous during 2001-2018. The spatial patterns of  $ET_a$  trend in spring  
448 and summer were similar to the annual changes in  $ET_a$ .  $ET_a$  decreased as  
449 well in the spring and summer season but at slower rates compared with the  
450 annual  $ET_a$ , however, only very weak trends were found in the autumn and

451 winter seasons.

452

## 453 **5 Data availability**

454 The dataset presented and analyzed in this article has been released and is

455 available for free download from the Science Data Bank

456 (<http://www.dx.doi.org/10.11922/sciencedb.t00000.00010>, (Han et al., 2020))

457 and from the National Tibetan Plateau Data Center

458 (<https://data.tpdac.ac.cn/en/data/5a0d2e28-ebc6-4ea4-8ce4-a7f2897c8ee6/>).

459 The dataset is published under the Creative Commons Attribution 4.0

460 International (CC BY 4.0) license.

461

## 462 **Acknowledgments**

463 This study was funded by the Second Tibetan Plateau Scientific Expedition  
464 and Research (STEP) program (grant no. 2019QZKK0103), the Strategic  
465 Priority Research Program of Chinese Academy of Sciences (XDA20060101),  
466 the National Natural Science Foundation of China (91837208, 41705005, and  
467 41830650). The CMFD data were obtained from the National Tibetan Plateau  
468 Data Center ([https://data.tpdac.ac.cn/en/data/8028b944-daaa-4511-8769-  
469 965612652c49/](https://data.tpdac.ac.cn/en/data/8028b944-daaa-4511-8769-965612652c49/)). MODIS data were obtained from the NASA Land Processes  
470 Distributed Active Archive Center (<https://lpdaac.usgs.gov/>). Global 1 km  
471 forest canopy height data were obtained from the Oak Ridge National  
472 Laboratory Distributed Active Archive Center for Biogeochemical Dynamics  
473 ([https://daac.ornl.gov/cgi-bin/dsviewer.pl?ds\\_id=1271](https://daac.ornl.gov/cgi-bin/dsviewer.pl?ds_id=1271)). The authors would like  
474 to thank all colleagues working at the observational stations on the TP for their  
475 maintenance of the instruments.

476

477

- 479 Chen, X., Z. Su, Y. Ma, S. Liu, Q. Yu, Z. Xu. 2014. Development of a 10-year (2001-2010) 0.1° data set  
480 of land-surface energy balance for mainland China. *Atmospheric Chemistry and Physics* 14(23):  
481 13097-13117.
- 482 Chen, X., Z. Su, Y. Ma, E. M. Middleton. 2019. Optimization of a remote sensing energy balance method  
483 over different canopy applied at global scale. *Agricultural and Forest Meteorology* 279: 107633-  
484 107633.
- 485 Chen, X., Z. Su, Y. Ma, K. Yang, B. Wang. 2013a. Estimation of surface energy fluxes under complex  
486 terrain of Mt. Qomolangma over the Tibetan Plateau. *Hydrol. Earth Syst. Sci.* 17(4): 1607-1618.
- 487 Chen, X., Z. Su, Y. Ma, K. Yang, J. Wen, Y. Zhang. 2013b. An Improvement of Roughness Height  
488 Parameterization of the Surface Energy Balance System (SEBS) over the Tibetan Plateau. *Journal*  
489 *of Applied Meteorology and Climatology* 52(3): 607-622.
- 490 Fisher, J. B., F. Melton, E. Middleton, C. Hain, M. Anderson, R. Allen, M. F. McCabe, S. Hook, D.  
491 Baldocchi, P. A. Townsend, A. Kilic, K. Tu, D. D. Miralles, J. Perret, J.-P. Lagouarde, D. Waliser, A.  
492 J. Purdy, A. French, D. Schimel, J. S. Famiglietti, G. Stephens, E. F. Wood. 2017. The future of  
493 evapotranspiration: Global requirements for ecosystem functioning, carbon and climate feedbacks,  
494 agricultural management, and water resources. *Water Resources Research* 53(4): 2618-2626.
- 495 Gao, Z. Q., C. S. Liu, W. Gao, N. B. Chang. 2011. A coupled remote sensing and the Surface Energy  
496 Balance with Topography Algorithm (SEBTA) to estimate actual evapotranspiration over  
497 heterogeneous terrain. *Hydrol. Earth Syst. Sci.* 15(1): 119-139.
- 498 Grant, A. L. M., P. J. Mason. 1990. Observations of boundary-layer structure over complex terrain.  
499 *Quarterly Journal of the Royal Meteorological Society* 116(491): 159-186.
- 500 Han, C., Y. Ma, X. Chen, Z. Su. 2016. Estimates of land surface heat fluxes of the Mt. Everest region  
501 over the Tibetan Plateau utilizing ASTER data. *Atmospheric Research* 168: 180-190.
- 502 Han, C., Y. Ma, X. Chen, Z. Su. 2017. Trends of land surface heat fluxes on the Tibetan Plateau from  
503 2001 to 2012. *International Journal of Climatology* 37(14): 4757-4767.
- 504 Han, C., Y. Ma, Z. Su, X. Chen, L. Zhang, M. Li, F. Sun. 2015. Estimates of effective aerodynamic  
505 roughness length over mountainous areas of the Tibetan Plateau. *Quarterly Journal of the Royal*  
506 *Meteorological Society* 141(689): 1457-1465.
- 507 Han, C., Y. Ma, B. Wang, L. Zhong, W. Ma, X. Chen, Z. Su. 2020. The estimated actual  
508 evapotranspiration over the Tibetan Plateau from 2001 to 2018. *VI. Science Data Bank.*  
509 <http://www.dx.doi.org/10.11922/sciencedb.t00000.00010>.
- 510 He, J., K. Yang, W. Tang, H. Lu, J. Qin, Y. Chen, X. Li. 2020. The first high-resolution meteorological  
511 forcing dataset for land process studies over China. *Scientific Data* 7(1): 25-25.
- 512 Immerzeel, W. W., L. P. H. van Beek, M. F. P. Bierkens. 2010. Climate Change Will Affect the Asian  
513 Water Towers. *Science* 328(5984): 1382 LP-1385.
- 514 Li, X., G. Cheng, S. Liu, Q. Xiao, M. Ma, R. Jin, T. Che, Q. Liu, W. Wang, Y. Qi, J. Wen, H. Li, G. Zhu,  
515 J. Guo, Y. Ran, S. Wang, Z. Zhu, J. Zhou, X. Hu, Z. Xu. 2013. Heihe Watershed Allied Telemetry  
516 Experimental Research (HiWATER): Scientific Objectives and Experimental Design. *Bulletin of the*  
517 *American Meteorological Society* 94(8): 1145-1160.
- 518 Li, X., L. Wang, D. Chen, K. Yang, A. Wang. 2014. Seasonal evapotranspiration changes (1983–2006)

519 of four large basins on the Tibetan Plateau. *Journal of Geophysical Research: Atmospheres* 119(23):  
520 13,13-79,95.

521 Liu, X., H. Zheng, M. Zhang, C. Liu. 2011. Identification of dominant climate factor for pan evaporation  
522 trend in the Tibetan Plateau. *Journal of Geographical Sciences* 21(4): 594-608.

523 Ma, N., J. Szilagyi, Y. Zhang, W. Liu. 2019. Complementary-Relationship-Based Modeling of Terrestrial  
524 Evapotranspiration Across China During 1982–2012: Validations and Spatiotemporal Analyses.  
525 *Journal of Geophysical Research: Atmospheres* 124(8): 4326-4351.

526 Ma, W., Y. Ma, H. Ishikawa. 2014. Evaluation of the SEBS for upscaling the evapotranspiration based  
527 on in-situ observations over the Tibetan Plateau. *Atmospheric Research* 138: 91-97.

528 Ma, Y., Z. Hu, Z. Xie, W. Ma, B. Wang, X. Chen, M. Li, L. Zhong, F. Sun, L. Gu, C. Han, L. Zhang, X.  
529 Liu, Z. Ding, G. Sun, S. Wang, Y. Wang, Z. Wang. 2020. A long-term (2005–2016) dataset of hourly  
530 integrated land–atmosphere interaction observations on the Tibetan Plateau. *Earth Syst. Sci. Data*  
531 12(4): 2937-2957.

532 Ma, Y., Z. Su, T. Koike, T. Yao, H. Ishikawa, K. i. Ueno, M. Menenti. 2003. On measuring and remote  
533 sensing surface energy partitioning over the Tibetan Plateau—from GAME/Tibet to CAMP/Tibet.  
534 *Physics and Chemistry of the Earth, Parts A/B/C* 28(1): 63-74.

535 Ma, Y., L. Zhong, B. Wang, W. Ma, X. Chen, M. Li. 2011. Determination of land surface heat fluxes over  
536 heterogeneous landscape of the Tibetan Plateau by using the MODIS and in situ data. *Atmos. Chem.*  
537 *Phys.* 11(20): 10461-10469.

538 Mauder, M., T. Foken. 2015. Eddy-Covariance Software TK3.

539 Moore, C. J. 1986. Frequency response corrections for eddy correlation systems. *Boundary-Layer*  
540 *Meteorology* 37(1): 17-35.

541 Oki, T., S. Kanae. 2006. Global Hydrological Cycles and World Water Resources. *Science* 313(5790):  
542 1068 LP-1072.

543 Pinker, R. T., I. Laszlo. 1992. Modeling Surface Solar Irradiance for Satellite Applications on a Global  
544 Scale. *Journal of Applied Meteorology* 31(2): 194-211.

545 Shi, H., T. Li, G. Wang. 2017. Temporal and spatial variations of potential evaporation and the driving  
546 mechanism over Tibet during 1961–2001. *Hydrological Sciences Journal* 62(9): 1469-1482.

547 Stull, R. B. (1988). An introduction to boundary layer meteorology. Dordrecht, Kluwer Academic  
548 Publishers.

549 Su, Z. 2002. The Surface Energy Balance System (SEBS) for estimation of turbulent heat fluxes. *Hydrol.*  
550 *Earth Syst. Sci.* 6(1): 85-100.

551 Szilagyi, J., R. Crago, R. Qualls. 2017. A calibration-free formulation of the complementary relationship  
552 of evaporation for continental-scale hydrology. *Journal of Geophysical Research: Atmospheres*  
553 122(1): 264-278.

554 Wang, B., Y. Ma, Z. Su, Y. Wang, W. Ma. 2020a. Quantifying the evaporation amounts of 75 high-  
555 elevation large dimictic lakes on the Tibetan Plateau. *Science Advances* 6(26): eaay8558.

556 Wang, G., S. Lin, Z. Hu, Y. Lu, X. Sun, K. Huang. 2020b. Improving Actual Evapotranspiration  
557 Estimation Integrating Energy Consumption for Ice Phase Change Across the Tibetan Plateau.  
558 *Journal of Geophysical Research: Atmospheres* 125(3): e2019JD031799-e032019JD031799.

559 Wang, K., J. Liu, X. Zhou, M. Sparrow, M. Ma, Z. Sun, W. Jiang. 2004. Validation of the MODIS global  
560 land surface albedo product using ground measurements in a semidesert region on the Tibetan

561 Plateau. *Journal of Geophysical Research: Atmospheres* 109(D5).

562 Webb, E. K., G. I. Pearman, R. Leuning. 1980. Correction of flux measurements for density effects due  
563 to heat and water vapour transfer. *Quarterly Journal of the Royal Meteorological Society* 106(447):  
564 85-100.

565 Xie, Z., Z. Hu, L. Gu, G. Sun, Y. Du, X. Yan. 2017. Meteorological Forcing Datasets for Blowing Snow  
566 Modeling on the Tibetan Plateau: Evaluation and Intercomparison. *Journal of Hydrometeorology*  
567 18(10): 2761-2780.

568 Xu, C. Y., V. P. Singh. 2005. Evaluation of three complementary relationship evapotranspiration models  
569 by water balance approach to estimate actual regional evapotranspiration in different climatic  
570 regions. *Journal of Hydrology* 308(1): 105-121.

571 Yang, K., H. Wu, J. Qin, C. Lin, W. Tang, Y. Chen. 2014. Recent climate changes over the Tibetan Plateau  
572 and their impacts on energy and water cycle: A review. *Global and Planetary Change* 112: 79-91.

573 Yang, W., X. Guo, T. Yao, K. Yang, L. Zhao, S. Li, M. Zhu. 2011. Summertime surface energy budget  
574 and ablation modeling in the ablation zone of a maritime Tibetan glacier. *Journal of Geophysical*  
575 *Research: Atmospheres* 116(D14).

576 Yao, T., H. Lu, W. Feng, Q. Yu. 2019. Evaporation abrupt changes in the Qinghai-Tibet Plateau during  
577 the last half-century. *Scientific Reports* 9(1): 20181-20181.

578 Yao, T., L. Thompson, W. Yang, W. Yu, Y. Gao, X. Guo, X. Yang, K. Duan, H. Zhao, B. Xu, J. Pu, A. Lu,  
579 Y. Xiang, D. B. Kattel, D. Joswiak. 2012. Different glacier status with atmospheric circulations in  
580 Tibetan Plateau and surroundings. *Nature Climate Change* 2(9): 663-667.

581 Zhang, C., F. Liu, Y. Shen. 2018a. Attribution analysis of changing pan evaporation in the Qinghai-  
582 Tibetan Plateau, China. *International Journal of Climatology* 38(S1): e1032-e1043.

583 Zhang, K., J. S. Kimball, R. R. Nemani, S. W. Running. 2010. A continuous satellite-derived global  
584 record of land surface evapotranspiration from 1983 to 2006. *Water Resources Research* 46(9).

585 Zhang, T., M. Gebremichael, X. Meng, J. Wen, M. Iqbal, D. Jia, Y. Yu, Z. Li. 2018b. Climate-related  
586 trends of actual evapotranspiration over the Tibetan Plateau (1961–2010). *International Journal of*  
587 *Climatology* 38(S1): e48-e56.

588 Zhang, Y., C. Liu, Y. Tang, Y. Yang. 2007. Trends in pan evaporation and reference and actual  
589 evapotranspiration across the Tibetan Plateau. *Journal of Geophysical Research: Atmospheres*  
590 112(D12).

591 Zhong, L., Y. Ma, Z. Hu, Y. Fu, Y. Hu, X. Wang, M. Cheng, N. Ge. 2019. Estimation of hourly land  
592 surface heat fluxes over the Tibetan Plateau by the combined use of geostationary and polar-orbiting  
593 satellites. *Atmos. Chem. Phys.* 19(8): 5529-5541.

594 Zhou, J., L. Wang, Y. Zhang, Y. Guo, D. He. 2016. Spatiotemporal variations of actual evapotranspiration  
595 over the Lake Selin Co and surrounding small lakes (Tibetan Plateau) during 2003–2012. *Science*  
596 *China Earth Sciences* 59(12): 2441-2453.

597 Zou, M., L. Zhong, Y. Ma, Y. Hu, Z. Huang, K. Xu, L. Feng. 2018. Comparison of Two Satellite-Based  
598 Evapotranspiration Models of the Nagqu River Basin of the Tibetan Plateau. *Journal of Geophysical*  
599 *Research: Atmospheres* 123(8): 3961-3975.

600

601

602 **List of tables**

603 Table 1: Input datasets used in this study. .... 23

604 Table 2: Station information. .... 24

605

606

607

608 Table 1: Input datasets used in this study.

<b>Variables</b>	<b>Data source</b>	<b>Availability</b>	<b>Temporal resolution</b>	<b>Spatial resolution</b>
Downward Shortwave	CMFD	1979 – 2018	3 hours	0.1°
Downward longwave	CMFD	1979 – 2018	3 hours	0.1°
Air temperature	CMFD	1979 – 2018	3 hours	0.1°
Specific humidity	CMFD	1979 – 2018	3 hours	0.1°
Wind velocity	CMFD	1979 – 2018	3 hours	0.1°
Land surface temperature	MOD11C3	2001 – now	Monthly	0.05°
Land surface emissivity	MOD11C3	2001 – now	Monthly	0.05°
Height of canopy	GLAS & SPOT	2000 - now	Monthly	0.01°
Albedo	MOD09CMG	2001 - now	Daily	0.05°
NDVI	MOD13C2	2001 - now	Monthly	0.05°
DEM	ASTER GDEM	-	-	30 m

609

610

611

612 Table 2: Station information.

<b>Station</b>	<b>Location</b>	<b>Elevation (m)</b>	<b>Land cover</b>
QOMS	28.21°N, 86.56°E	4276	Gravel
NAMORS	30.46°N, 90.59°E	4730	Grassy marshland
SETORS	29.77°N, 94.73°E	3326	Grass land
NADORS	33.39°N, 79.70°E	4264	Sparse grass-Gobi
MAWORS	38.41°N, 75.05°E	3668	Sparse grass-Gobi
BJ	31.37°N, 91.90°E	4509	Sparseness meadow

613

614

615



616 **List of figures**

617 Figure 1: Locations of the six flux tower sites (marked by pentagrams) on the  
618 TP. The legend of the color map is elevation above mean sea level in meters.  
619 ..... 26

620 Figure 2: SEBS-estimated and EC-observed monthly  $ET_a$  at the six stations (a-  
621 f) on the TP in years when the latter observations were available. RMSE is the  
622 root-mean-square error, MB is the mean bias, and R is the correlation  
623 coefficient ..... 27

624 Figure 3: Spatial distribution of the SEBS-estimated multiyear (2001-2018)  
625 average annual  $ET_a$ . ..... 28

626 Figure 4: Spatial distributions of the SEBS-estimated multiyear (2001-2018)  
627 average seasonal  $ET_a$  (mm/season) values over the TP. (a) spring, (b) summer,  
628 (c) autumn, (d) winter. .... 29

629 Figure 5: Spatial distribution of annual  $ET_a$  linear trend on the TP from 2001 to  
630 2018. The stippling indicates the trends that pass the t-test ( $p < 0.05$ ). ..... 30

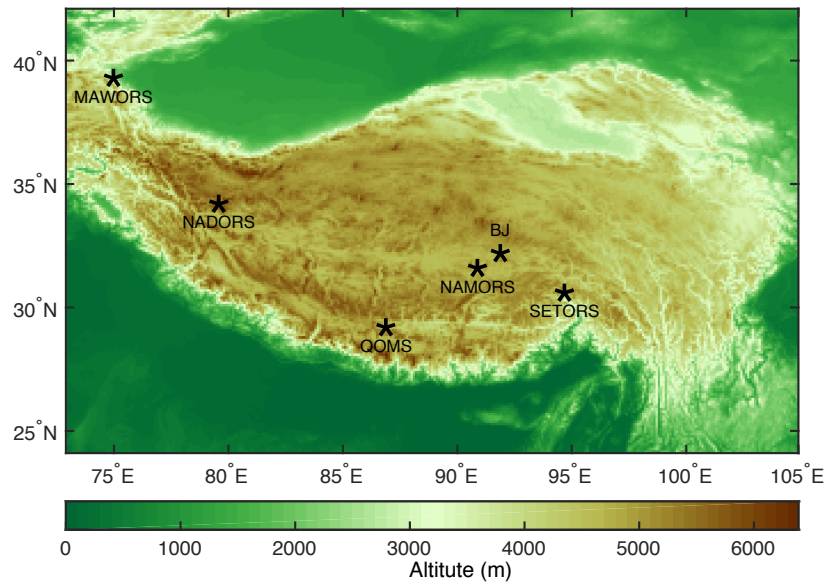
631 Figure 6: Spatial distributions of seasonal  $ET_a$  linear trends on the TP from 2001  
632 to 2018: (a) annual, (b) spring, (c) summer, (d) autumn, (e) winter. The stippling  
633 indicates the trends that pass the t-test ( $p < 0.05$ ). ..... 31

634 Figure 7: Anomalies of the domain-averaged annual  $ET_a$  of the entire TP, the  
635 western TP ( $\text{lon} < 90^\circ \text{ E}$ ), and the eastern TP ( $\text{lon} > 90^\circ \text{ E}$ ), respectively (a).  
636 Domain-averaged seasonal  $ET_a$  anomalies over the entire TP (b). The dashed  
637 straight lines indicate linear trends during 2001-2018, and  $k$  is the slope of the  
638 straight line. .... 32

639 Figure 8: Domain-averaged anomalies of annual  $R_n$  (a), precipitation (b), and  
640 temperature (c) over the entire TP, the western TP ( $\text{lon} < 90^\circ \text{ E}$ ), and the eastern  
641 TP ( $\text{lon} > 90^\circ \text{ E}$ ), respectively. The dashed straight lines indicate linear trends  
642 during 2001-2018, and  $k$  is the slope of the straight line. .... 33

643

644



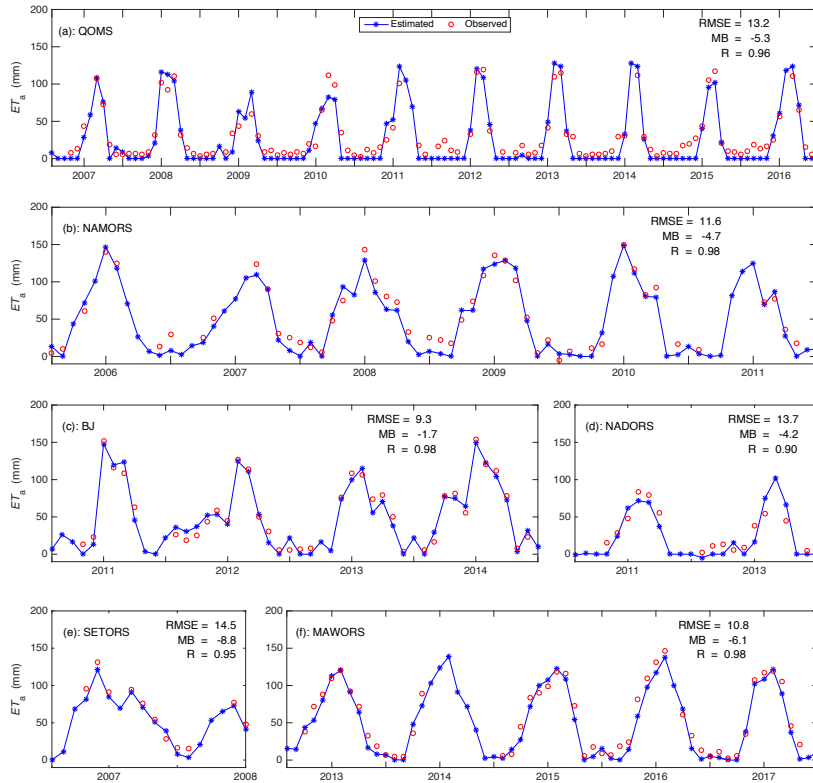
645

646 Figure 1: Locations of the six flux tower sites (marked by pentagrams) on the

647 TP. The legend of the color map is elevation above mean sea level in meters.

648

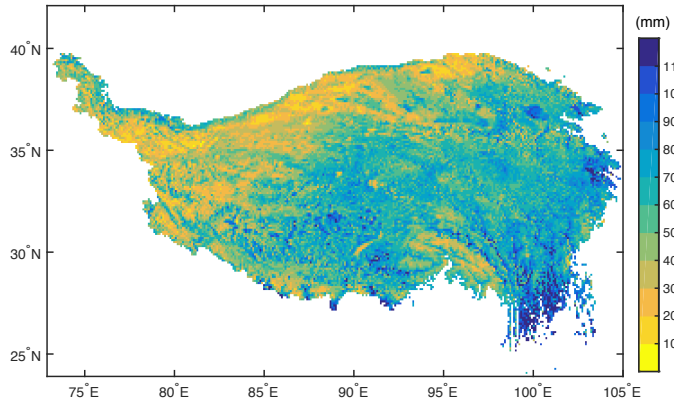
649



650

651 Figure 2: SEBS-estimated and EC-observed monthly  $ET_a$  at the six stations  
652 (a-f) on the TP in years when the latter observations were available. RMSE is  
653 the root-mean-square error, MB is the mean bias, and R is the correlation  
654 coefficient.  
655

656



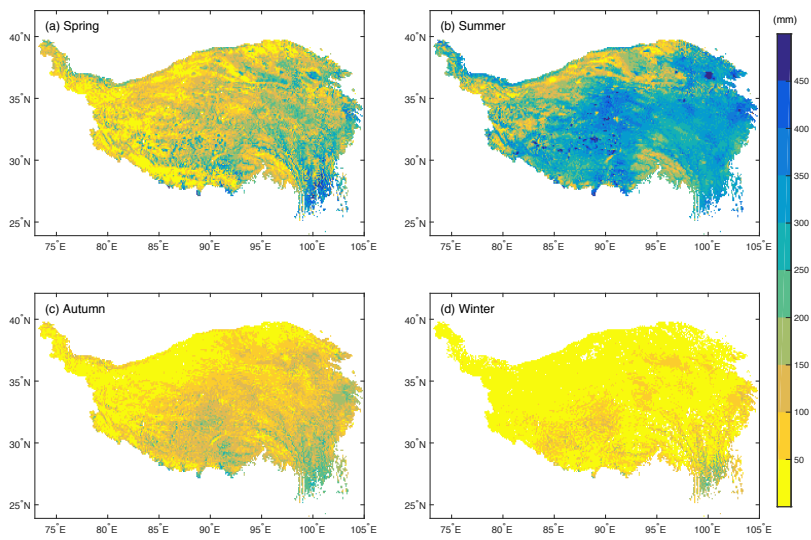
657

658 Figure 3: Spatial distribution of the SEBS-estimated multiyear (2001-2018)

659 average annual  $ET_a$ .

660

661



662

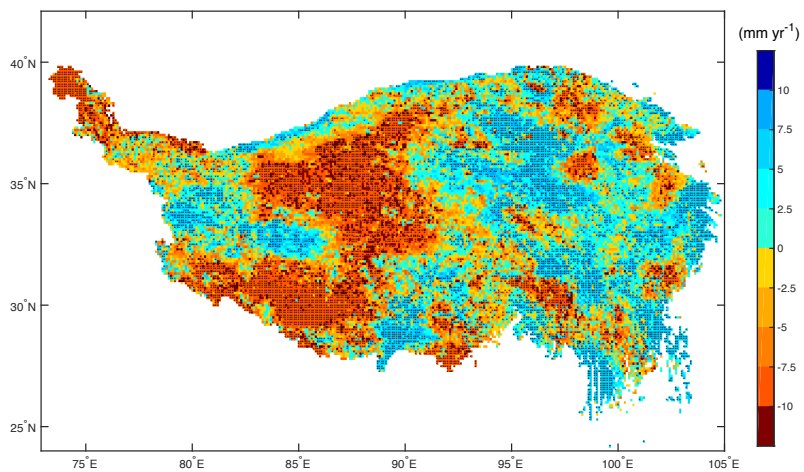
663 Figure 4: Spatial distributions of the SEBS-estimated multiyear (2001-2018)

664 average seasonal  $ET_a$  (mm/season) values over the TP. (a) spring, (b)

665 summer, (c) autumn, (d) winter.

666

667



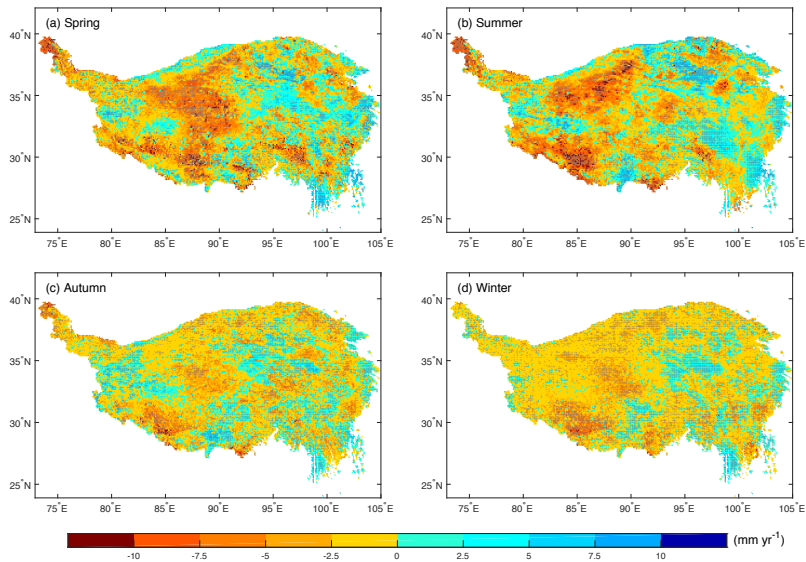
668

669 Figure 5: Spatial distribution of annual  $ET_a$  linear trend on the TP from 2001 to

670 2018. The stippling indicates the trends that pass the t-test ( $p < 0.05$ ).

671

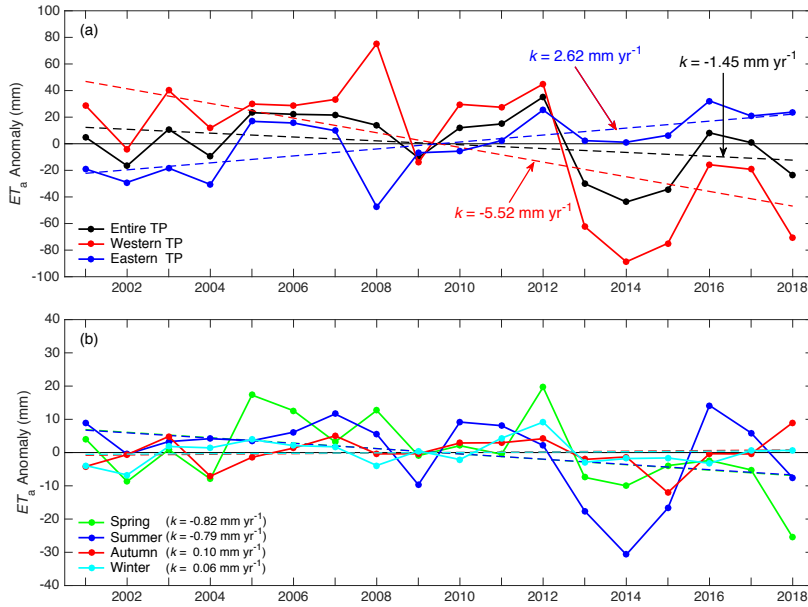
672



673

674 Figure 6: Spatial distributions of seasonal  $ET_a$  linear trends on the TP from  
675 2001 to 2018: (a) annual, (b) spring, (c) summer, (d) autumn, (e) winter. The  
676 stippling indicates the trends that pass the  $t$ -test ( $p < 0.05$ ).  
677

678



679

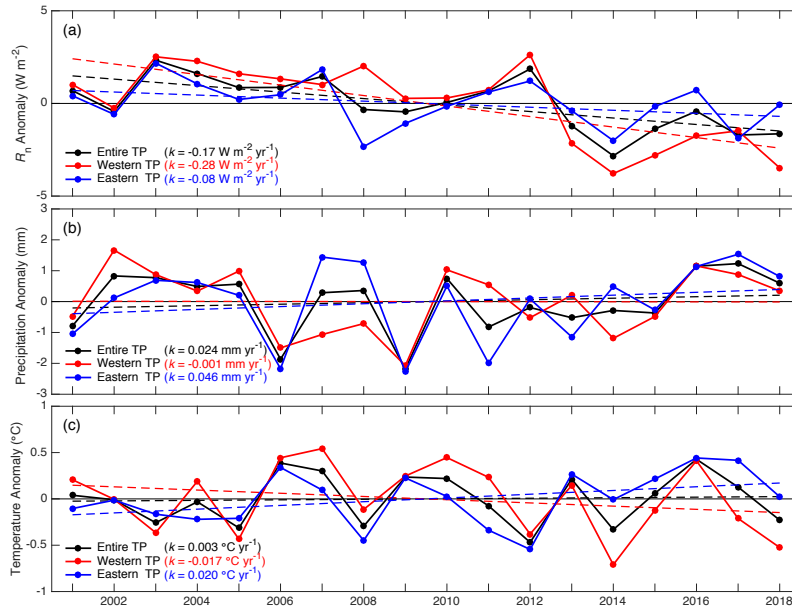
680 Figure 7: Anomalies of the domain-averaged annual  $ET_a$  of the entire TP, the  
681 western TP (lon < 90° E), and the eastern TP (lon > 90° E), respectively (a).  
682 Domain-averaged seasonal  $ET_a$  anomalies over the entire TP (b). The dashed  
683 straight lines indicate linear trends during 2001-2018, and  $k$  is the slope of the  
684 straight line.

685

686



687



688

689 Figure 8: Domain-averaged anomalies of annual  $R_n$  (a), precipitation (b), and

690 temperature (c) over the entire TP, the western TP ( $lon < 90^{\circ} E$ ), and the

691 eastern TP ( $lon > 90^{\circ} E$ ), respectively. The dashed straight lines indicate

692 linear trends during 2001-2018, and  $k$  is the slope of the straight line.

693